

## Article

# Enhancing the Potentiometric H<sub>2</sub> Sensing of Pr<sub>0.1</sub>Ce<sub>0.9</sub>O<sub>2-δ</sub> Using Fe<sub>2</sub>O<sub>3</sub> Surface Modification

Liang Wang and Jianxin Yi \*

State Key Laboratory of Fire Science, Department of Safety Science and Engineering, University of Science and Technology of China, Hefei 230026, China; wloro@mail.ustc.edu.cn

\* Correspondence: yjx@ustc.edu.cn; Tel.: +86-551-63607817

**Abstract:** Monitoring the concentration of hydrogen is very important as it is a flammable and explosive gas. Non-Nernstian potentiometric hydrogen sensors hold promising potentials for the sensitive detection of hydrogen. This paper reports the improved H<sub>2</sub>-sensing performance of a mixed oxide ion-electron conducting (MIEC) Pr<sub>0.1</sub>Ce<sub>0.9</sub>O<sub>2-δ</sub> (PCO) electrode using Fe<sub>2</sub>O<sub>3</sub> surface modification. The Fe<sub>2</sub>O<sub>3</sub>-modified PCO exhibited a high response of −184.29 mV to 1000 ppm H<sub>2</sub> at 450 °C. The response values exhibited a linear or logarithmic dependence on the H<sub>2</sub> concentration for below or above 20 ppm, respectively. A sensitivity of −74.9 mV/decade in the concentration range of 20–1000 ppm was achieved, and the theoretical limit of detection was calculated to be 343 ppb. Moreover, a power-law relationship between the response time and the concentration value was also found. Electrochemical impedance analyses revealed that the excellent H<sub>2</sub>-sensing performance may be attributed to the large ratio of the electrochemical activity of the hydrogen oxidation reaction (HOR) over the oxygen exchange reaction (OER). In addition, the distribution of relaxation time (DRT) results reveal that the enhanced electrochemical kinetics caused by H<sub>2</sub> presence in air is mainly related to acceleration of the electrode surface processes.

**Keywords:** solid electrolyte; potentiometric gas sensor; Fe<sub>2</sub>O<sub>3</sub> surface modification; electrochemical activity



**Citation:** Wang, L.; Yi, J. Enhancing the Potentiometric H<sub>2</sub> Sensing of Pr<sub>0.1</sub>Ce<sub>0.9</sub>O<sub>2-δ</sub> Using Fe<sub>2</sub>O<sub>3</sub> Surface Modification. *Chemosensors* **2023**, *11*, 250. <https://doi.org/10.3390/chemosensors11040250>

Academic Editor: Tatsuo Yoshinobu

Received: 27 March 2023

Revised: 10 April 2023

Accepted: 11 April 2023

Published: 17 April 2023



**Copyright:** © 2023 by the authors. Licensee MDPI, Basel, Switzerland. This article is an open access article distributed under the terms and conditions of the Creative Commons Attribution (CC BY) license (<https://creativecommons.org/licenses/by/4.0/>).

## 1. Introduction

Hydrogen (H<sub>2</sub>) is a very promising clean and renewable fuel with abundant reserves and high energy density which is widely utilized in many fields such as spaceships and many industrial sectors [1–3]. However, H<sub>2</sub> is one of the most important conventional fire detection marker gases due to its many unusual properties such as its lack of color or odor, its ultra-low ignition energy of only 0.02 mJ and its very large flammable range (4–75%) [4,5]. During the storage and usage of H<sub>2</sub>, the hydrogen embrittlement phenomenon can lead to the failure of the protective layer and cause hydrogen spillage or even leakage, which can lead to fire and explosion accidents and pose a serious threat to the safety of human life and property [6]. Therefore, it is important for the popularization and development of the use of hydrogen energy to research low-concentration hydrogen sensors that can detect ppm or even ppb levels, in order to warn about hydrogen leaks as soon as possible [7]. In addition, low-concentration hydrogen detection has important potential value in the fields of earthquake early warning and respiratory gas disease monitoring [8,9].

Currently, the most widely used sensors are metal oxide semiconductors, catalytic combustion and electrochemical gas sensors. Semiconductor sensors can detect hydrogen at the ppm level, but with poor selectivity. Catalytic sensors are mainly used to detect the hydrogen in air at pre-explosive concentrations of 0.1–2% and have the advantages of low operating temperature and high selectivity [10,11]. Electrochemical non-Nernstian potentiometric gas sensors with simple configurations, wider operating temperatures, high sensitivity and low cost have attracted considerable attention from researchers. Solid

electrolyte, sensitive electrode (SE) and reference electrode (RE) are generally the three important components of a non-Nernstian-type potentiometric gas sensor [12]. This type of sensor responds to the measured gas through changes in electrode potential caused by the competition between various electrochemical reactions proceeding over the three-phase boundary (TPB, which is the boundary between the electrolyte, electrode and gas), which do not follow the Nernst equation [13–15]. Three different mechanisms, namely the electrochemical, the electrical and the surface electrostatic mechanism, have been proposed for non-Nernstian sensing behavior, among which the electrochemical one has been very often adopted, according to mixed-potential theory [16–18]. Over the past decades, researchers have done a great deal to develop high-performance non-Nernstian gas sensors. It was found that SE materials play a crucial role in determining the sensor response. For example, Miura et al. developed a  $\text{ZrSiO}_4(+\text{Au})$  sensitive electrode material for detecting  $\text{H}_2$ , which had a high sensitivity and good selectivity for  $\text{H}_2$  [15]. Zhang et al. reported a novel  $\text{La}_{0.8}\text{Sr}_{0.2}\text{Cr}_{0.5}\text{Fe}_{0.5}\text{O}_{3-\delta}$  sensitive material, which had a fast response, high sensitivity and selectivity to  $\text{H}_2$  [14]. Lu et al. fabricated a  $\text{NH}_3$  sensor based on a metal-oxide ( $\text{NiO}$ ,  $\text{SnO}_2$ ,  $\text{WO}_3$ )-modified  $\text{FeVO}_4$  sensitive electrode material, which had the advantages of a short response time, short recovery time and good oxygen resistance [19]. While a great amount of sensitive electrode materials has been investigated, the optimal potential sensing performance has not yet been observed.

Depending on the widely adopted mixed-potential principle, the ratio of electrochemical activity of the SE material to the interfacial electrochemical reactions proceeding over the TPB can serve as a valid indicator of the sensor response. A large activity ratio of hydrogen oxidation over oxygen reduction favors a high response to hydrogen [20,21]. In this sense, regulating the electrochemical activities of the SE material could tune the sensor response, which provides a strategy to select sensitive electrode materials rationally. For instance, Zhang et al. investigated the relationship between the mixed-potential hydrogen response and the electrochemical activity of perovskite oxides, which showed that the activity ratio can be used as a response descriptor potentially applicable to different materials and target gases [16]. In addition, Nicollet et al. recently found that the oxygen surface exchange (oxygen reduction/evolution) kinetics of MIEC oxides is highly dependent upon surface acidity, and infiltrating strongly acidic oxides onto the material surface may dramatically decrease the oxygen exchange kinetics [22]. This finding suggests that there is a possibility to boost the potentiometric gas sensing performance of MIEC electrodes using strongly acidic oxide surface modification. Although oxide surface modification has been used to prepare composite electrode materials [12], its effect on non-Nernstian gas sensing properties and the underlying mechanism remains unclear.

This work studied the influence of strongly acidic  $\text{Fe}_2\text{O}_3$  surface modification on the potentiometric gas sensing performance of a model MIEC oxide,  $\text{Pr}_{0.1}\text{Ce}_{0.9}\text{O}_{2-\delta}$  (PCO). Results show that compared with pure PCO, the  $\text{Fe}_2\text{O}_3$ -modified sample exhibited a markedly enhanced  $\text{H}_2$  sensing performance. The excellent  $\text{H}_2$  sensing was ascribed to a large electrochemical activity ratio, and the enhanced electrochemical performance was associated with the acceleration of electrode surface processes.

## 2. Materials and Methods

### 2.1. Chemicals

Praseodymium nitrate ( $\text{Pr}(\text{NO}_3)_3 \cdot 6\text{H}_2\text{O}$ ) was purchased from Shanghai Aladdin Biochemical Technology. Iron nitrate ( $\text{Fe}(\text{NO}_3)_3 \cdot 9\text{H}_2\text{O}$ ), cerium nitrate ( $\text{Ce}(\text{NO}_3)_3 \cdot 6\text{H}_2\text{O}$ ), ethylene glycol (EG) and citric acid (CA) were purchased from Sinopharm Chemical Reagent, China. No further purification of these reagents was required, and they all reached analytical purity.

### 2.2. Materials Synthesis and Sensors Preparation

An adjusted Pechini-type sol-gel approach was used to obtain the PCO powder.  $\text{Pr}(\text{NO}_3)_3 \cdot 6\text{H}_2\text{O}$ ,  $\text{Ce}(\text{NO}_3)_3 \cdot 6\text{H}_2\text{O}$ , EG and CA were mixed according to the molar ratio of

1:1:2:2 to form the precursor solution. This solution was stirred and heated to 80 °C until the formation of a yellow sol, which was dried overnight at 110 °C, and finally sintered in a muffle furnace for 5 h under 700 °C to obtain a reddish-brown powder.

All the solid electrolytes in this experiment were square YSZ plates (yttria-stabilized zirconia) with a size of 13 mm × 13 mm × 0.25 mm, which were purchased from Hefei Kejing, China. Pt paste (PE-Pt-7840, Sino-Platinum Metals, Kunming, China) was painted on both sides of the YSZ as a current collector and RE, respectively, and it was strip-shaped with a size of 1 mm × 3 mm. Then, Pt wires were adhered to the Pt strips by using high-temperature Pt paste and finally calcined for 30 min at 1000 °C. We mixed the organic solvent ( $\alpha$ -terpineol and ethyl cellulose) with the prepared PCO powder at a mass ratio of 1:1 and ground it for 2 h to obtain the SE pastes, which were subsequently painted on the side of the electrolyte opposite to the RE, and finally sintered for 2 h at 900 °C. The diameter of all SE was 3 mm and the distance between them was ~5 mm. To obtain the Fe<sub>2</sub>O<sub>3</sub>-modified electrodes, which was named PCO-Fe<sub>2</sub>O<sub>3</sub>, 0.4 M precursor iron nitrate solution was prepared. Then, 5  $\mu$ L of the solution was dropped onto the surface of the PCO electrode using a pipette. After the surface modification was completed, samples were dried for 0.5 h at 100 °C, and finally sintered for 1 h in an atmosphere at 600 °C.

Using similar procedures, symmetrical electrodes for the electrochemical tests were also prepared by painting identical SE pastes symmetrically on different sides of the YSZ substrate, followed by sintering.

### 2.3. Characterization and Gas Sensing Measurements

The phase structure and crystal composition of PCO and PCO-Fe<sub>2</sub>O<sub>3</sub> electrodes sintered on YSZ were obtained through the X-ray powder diffraction (XRD) technique with a TTR-III diffractometer (Rigaku Corporation, Tokyo, Japan), using Cu K $\alpha$  radiation and a 2 $\theta$  collection range of 20°–90°. The microstructure of the electrodes was observed using a cold field emission scanning electron microscope (SEM, SU8220) equipped with an Oxford Aztec series X-ray spectrometer. The elemental composition of the electrodes was observed using X-ray photoelectron spectroscopy (XPS, ESCLAB 250) which used Al K $\alpha$  as the excitation source and used the C1s of binding energy at 284.8 eV for energy calibration.

A home-made two-chamber device was used to obtain the pristine response values for these sensitive electrodes, the details of which can be found in the previous work of our group [18]. In this method, high-temperature silver paste (DAD-87, Shanghai Research Institute of Synthetic Resins, Shanghai, China) was used to glue the YSZ substrate to the quartz tube, thereby forming two separate chambers. Since the SE and RE were located at opposing sides of the YSZ, the atmosphere in the SE and RE can be regulated separately. During the test, the chamber in which the SE was located was alternately introduced into the mixture of air/test gas and air, while the atmosphere in the chamber where the RE was located was always air. In order to obtain the required test gas concentrations for the experiment, we mixed dry air with standard gas (H<sub>2</sub>, NO<sub>2</sub>, CO, NH<sub>3</sub>, C<sub>7</sub>H<sub>8</sub>, H<sub>2</sub>S and CH<sub>4</sub>), using N<sub>2</sub> as the equilibrium gas. All gases were purchased from Nanjing Special Gases. The flow rate of each gas path was controlled using a mass flow meter (MFC, CS200, Beijing Seven-star Electronics, Beijing, China) and the total flow rate for the chambers of SE and RE was 200 mL/min.

The SE and RE were linked to the positive and negative terminals of an Agilent 34972A data acquisition unit to measure the response signal of the sensor, i.e., the open circuit voltage (OCV) between the SE and RE. In this paper,  $\Delta V = V_{\text{gas}} - V_{\text{air}}$  is defined as the response value of the sensor, where  $V_{\text{gas}}$  and  $V_{\text{air}}$  represent the open circuit voltage between the SE and RE when the SE is exposed to the mixture of test gas/air and to the air, respectively. The linear fit slope of the dependence function of the response value on the test gas concentration or logarithm concentration is taken as the sensitivity (S). Response time is defined as the time taken from when SE is exposed to the test gas to when the change in OCV reaches 90% of the response value, while recovery time is defined as the time taken between when the SE is exposed to air again and when the change in OCV

reaches 10% of the response value. The lower detection limit (LOD) is calculated by the following formula:

$$\text{LOD} = 3 \text{ rms}/S \quad (1)$$

where rms is the standard deviation of the base OCV and S represents sensitivity [23]. Humid gas was obtained by bubbling the gas through deionized water or a saturated salt solution ( $\text{MgCl}_2/\text{NaBr}$  saturated solution) and the relative humidity of the gas was tested using a hygrometer (Testo 605-H1).

#### 2.4. Electrochemical Analysis Methods

Electrochemical impedance spectroscopy (EIS) was conducted on samples with symmetrical electrodes of the SE and a Pt RE with an electrochemical workstation (VersaSTAT 3). During the EIS test, the frequency range and amplitude were set to 0.01 Hz–1 MHz and 20 mV, respectively. Both SEs were exposed to the same atmosphere (air or  $\text{H}_2/\text{air}$ ). ZSimpwin software was used to fit the data obtained from the impedance test, wherein an equivalent circuit composed of three R-CPE elements connected in series was used. The distribution of relaxation time (DRT) is a powerful technique that allows the separation of different key electrochemical reaction steps [18]. The impedance data obtained from measurements in air or  $\text{H}_2/\text{air}$  were transformed into a function of time constants  $\tau$  for DRT analysis. For the DRT analysis, the value of the regularization parameter  $\lambda$  was set to 0.001.

### 3. Results

#### 3.1. Characterization Results of Materials

The diffraction peaks of PCO are in perfect agreement with those in the standard card (JCPDS No.:43-1002), indicating a single-phase fluorite crystal structure, as shown in the XRD pattern of Figure 1. The XRD patterns of the  $\text{PCO-Fe}_2\text{O}_3$  samples are similar to that of PCO, and the presence of the oxide modifier was not detected, probably due to the relatively low loading or small particle size.

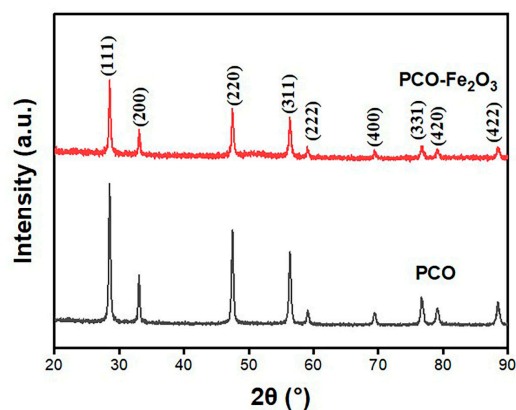
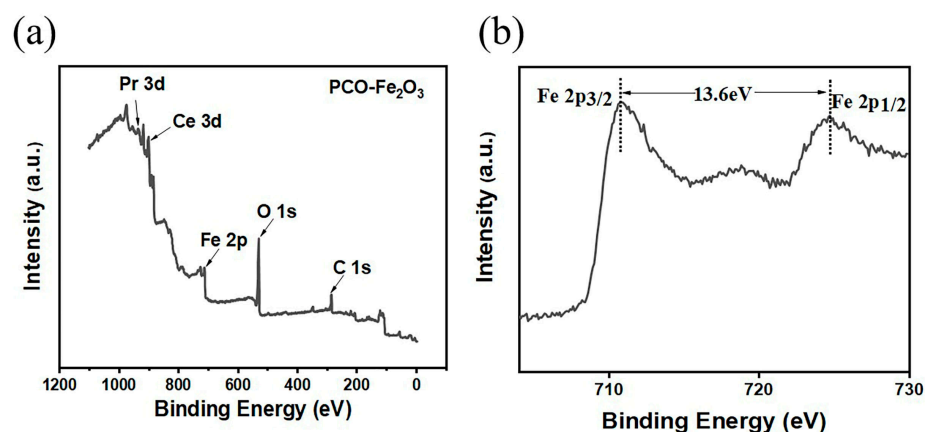


Figure 1. XRD patterns for PCO and  $\text{PCO-Fe}_2\text{O}_3$ .

XPS was used for the purpose of analyzing whether  $\text{PCO-Fe}_2\text{O}_3$  contains other impurity elements and the oxidation state of the modified metal ions, which is shown in Figure 2. Figure 2a shows that  $\text{PCO-Fe}_2\text{O}_3$  was composed of only Ce, Pr, Fe and O, without the presence of any other elements except C. Figure 2b shows Fe 2p<sub>3/2</sub>, Fe 2p<sub>1/2</sub> and a satellite peak composed of the Fe 2p spectrum. The spacing between the Fe 2p<sub>3/2</sub> and Fe 2p<sub>1/2</sub> doublets is 13.6 eV, and the satellite peak is located at 718 eV. This satellite peak has been observed in other studies and can be used as an indication of the formation of  $\text{Fe}_2\text{O}_3$  [24–26].

The SEM images presented in Figure 3a,b show that the electrode sintered on YSZ was mainly composed of particles with a size ranging from several tens of nanometers

to a few micrometers. Some pores can be observed among the particles, which facilitate gas diffusion. Figure 3c–f shows the EDS analysis results of PCO-Fe<sub>2</sub>O<sub>3</sub>. The modified Fe elements are uniformly distributed on the SE surface, confirming a well-dispersed composite synthesis. In addition, Figure S1a–d also gives the cross-sectional EDS mapping of PCO-Fe<sub>2</sub>O<sub>3</sub>, indicating that Fe<sub>2</sub>O<sub>3</sub> is present evenly not only on the surface of PCO but also inside PCO. These results reveal that Fe<sub>2</sub>O<sub>3</sub> was successfully formed on the PCO surface but likely had a very fine particle size.



**Figure 2.** XPS spectra for PCO-Fe<sub>2</sub>O<sub>3</sub>. (a) Survey spectrum; (b) Fe 2p for PCO-Fe<sub>2</sub>O<sub>3</sub>.

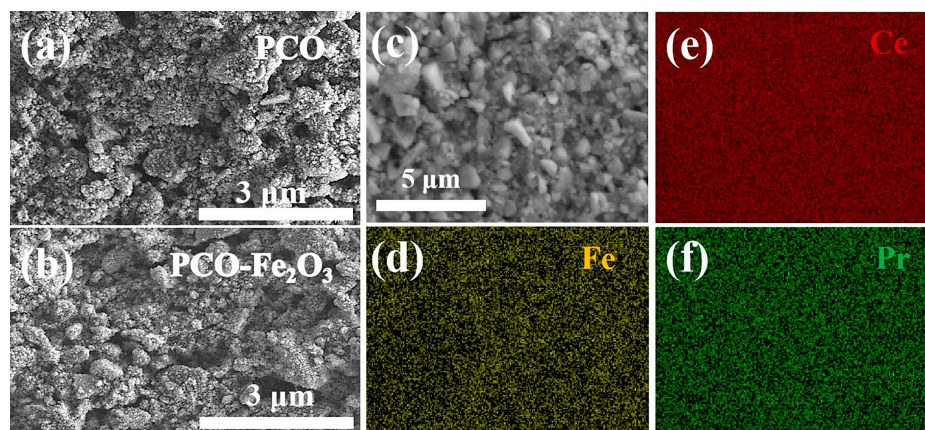


**Figure 3.** Surface SEM pictures for (a) PCO and (b) PCO-Fe<sub>2</sub>O<sub>3</sub>, (c–f) EDS spectrum of PCO-Fe<sub>2</sub>O<sub>3</sub>.

### 3.2. Sensing Performance

The pristine responses of the PCO-Fe<sub>2</sub>O<sub>3</sub> and PCO sensors were measured in a two-chamber mode by exposing the SE to base air or test gas/air mixture and the Pt RE to an air reference. The dynamic variation of the response values of the PCO and PCO-Fe<sub>2</sub>O<sub>3</sub> sensors with the increasing H<sub>2</sub> concentration at 450 °C and 500 °C are clearly observed in Figure 4. When SEs were exposed to only air, the base OCV for all the sensors remained at ~0. The OCV shifted negatively and approached a steady value when exposing SEs to H<sub>2</sub>. While the SEs atmosphere was again switched back to base air, the OCV increased rapidly and returned to the initial value. Clearly, all the sensors exhibited negative responses to H<sub>2</sub>. The OCV variation became more pronounced and the response increased with the increasing H<sub>2</sub> concentration. Under the tested conditions, the variation of OCV for PCO-Fe<sub>2</sub>O<sub>3</sub> was significantly larger than that for PCO, indicating that the Fe<sub>2</sub>O<sub>3</sub> modification successfully improved the response value. Note that the increase in response with the decrease in temperature has similarly been observed for other non-Nernstian gas sensors [12,14,27–29]. The temperature dependence of the response is a result of the joint effects of many affecting

factors, including the electrochemical reaction mechanism and heterogeneous catalytic activities, which are also a function of temperature [29].

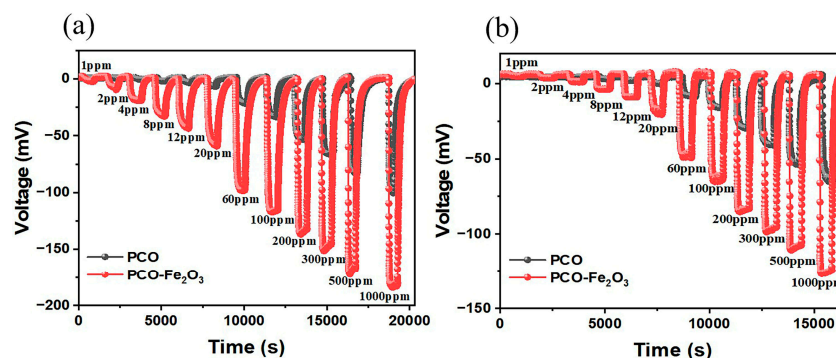


**Figure 4.** Dynamic response of sensors to  $H_2$  at (a) 450 °C and (b) 500 °C.

The response values of the PCO- $Fe_2O_3$  and PCO sensors as a function of  $H_2$  concentration or logarithm  $H_2$  concentration are shown in Figure 5. It can be directly observed that the response values of the PCO- $Fe_2O_3$  sensor to  $H_2$  are much greater than that of the PCO one, regardless of whether the  $H_2$  concentrations were low or high. The lowest  $H_2$  concentration in the experiment was measured at 1 ppm, and the response of PCO- $Fe_2O_3$  to 1 ppm  $H_2$  was  $-3.9$  mV, while PCO had almost no response to 1 ppm  $H_2$ . The response values of the two sensors showed a different dependence on the  $H_2$  concentration in the region of low and high  $H_2$  concentrations, respectively, i.e., the response values showed a linear relationship with the  $H_2$  concentration in the region of 1–20 ppm, while the response values showed a linear relationship with the logarithm  $H_2$  concentration in the region of 20–1000 ppm. For PCO- $Fe_2O_3$ , sensitivities of  $-2.97$  mV/ppm and  $-74.9$  mV/decade were obtained in the low and high  $H_2$  concentration ranges, respectively, which were 7.4 and 1.3 times greater than those for PCO in the same concentration range. In addition, the LOD for PCO- $Fe_2O_3$  was calculated to be 343 ppb, which is around 3.5 times lower than that of PCO (1.2 ppm). Similar concentration dependence has often been observed in other systems, and this is in accordance with the mixed-potential sensing mechanism.

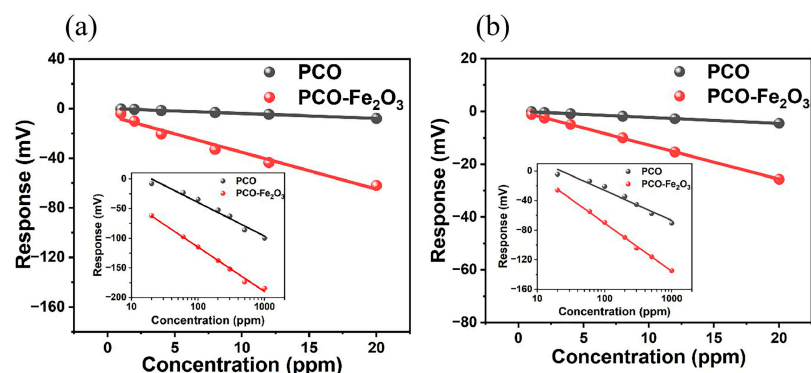


**Figure 5.** The function between the  $H_2$  concentration and the response value of PCO- $Fe_2O_3$  and PCO sensors at (a) 450 °C and (b) 500 °C. The insets display the function between the logarithmic  $H_2$  concentration and the response value of sensors.

The relationship between response time and recovery time with the concentrations of  $H_2$  for the PCO- $Fe_2O_3$  sensor was also studied, as shown in Figure 6. It can be observed that the response time reduces quickly with the increase in  $H_2$  concentration in the range of 20–300 ppm, while in a higher concentration range, the response time reduces slowly with the increase in  $H_2$  concentration and remains almost constant (Figure 6a). The response time declined with the rising temperature, with a value of 32 s and 22 s for 1000 ppm  $H_2$  at 450 °C and 500 °C, respectively. A power-law relationship between response time and

H<sub>2</sub> concentration on the log-log scale. Such behavior has also been observed in previous studies, agreeing with a theoretical simulation according to a mixed-potential sensing mechanism [27]. For recovery time, the variation with H<sub>2</sub> concentration was similar to that of the response time at 450 °C, while at 500 °C, the recovery time reduced slowly with the increase in H<sub>2</sub> concentration in the tested concentration range. The recovery time also decreased with an increasing temperature, with a value of 322 s and 122 s for 1000 ppm H<sub>2</sub> at 450 °C and 500 °C, respectively, which is much longer than the response time.

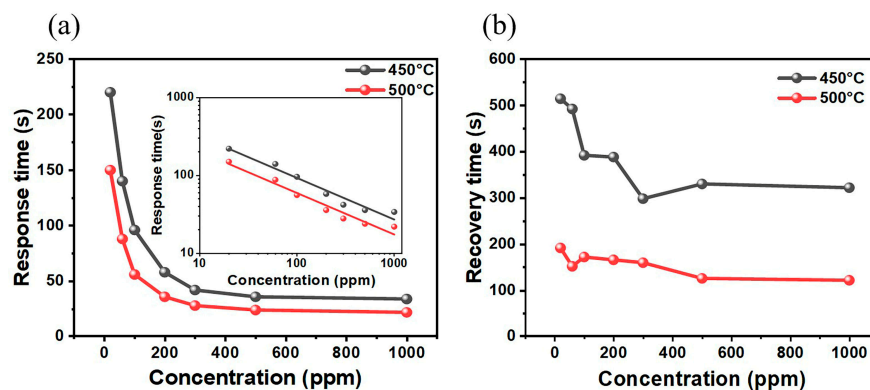


**Figure 6.** The relationship between (a) response time and (b) recovery time with the concentrations of H<sub>2</sub> for a PCO-Fe<sub>2</sub>O<sub>3</sub> sensor at 450 °C and 500 °C. The inset in (a) illustrates the response time as a function of the H<sub>2</sub> concentration on the log-log scale.

Figure 7 compares the response of PCO-Fe<sub>2</sub>O<sub>3</sub> towards different gases at 500 °C. PCO-Fe<sub>2</sub>O<sub>3</sub> responded most sensitively to H<sub>2</sub> and moderately to CO and C<sub>7</sub>H<sub>8</sub> but exhibited a rather small response to the other gases (NO<sub>2</sub>, NH<sub>3</sub>, H<sub>2</sub>S and CH<sub>4</sub>). Apparently, the PCO-Fe<sub>2</sub>O<sub>3</sub> sensor has excellent selectivity for H<sub>2</sub>, with particular regard to CH<sub>4</sub>, H<sub>2</sub>S, NH<sub>4</sub> and NO<sub>2</sub>. Humidity tolerance is also one important performance indicator of gas sensors. As shown in Figure 8a,b, the basic OCV of the PCO-Fe<sub>2</sub>O<sub>3</sub> sensor remained almost constant as the relative humidity (RH) of the base gas varied in the range of 2.8–99%. The H<sub>2</sub> response value decreased slightly with the increase in RH, and only an ~13.4% reduction was observed as RH increased from 2.8% to 99%. Repeatability is of significance for the practical application of gas sensors. As shown in Figure 8c, by alternately switching the test gas between air and the 300 ppm H<sub>2</sub>/air mixture, the response transients can be reproduced very well. The OCV varied by a similar magnitude in each cycle of the H<sub>2</sub> response and can be restored to the baseline upon H<sub>2</sub>'s removal from air, indicating the excellent repeatability of the measurements. Figure 8d presents a 15-day test of the PCO-Fe<sub>2</sub>O<sub>3</sub> sensor at 500 °C for 300 ppm H<sub>2</sub>. The response fluctuated between −97.32 mV and −107.88 mV, with a maximal variation of only 9.7%, revealing the good stability of the sample within the experimental period.

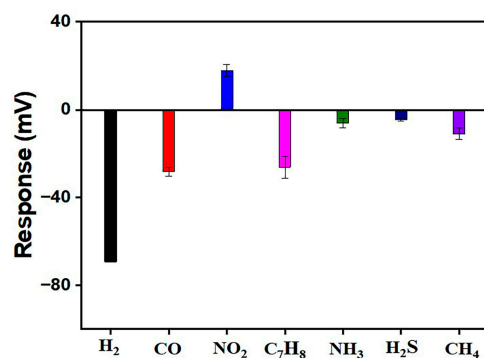


**Figure 7.** Comparison of response values of PCO-Fe<sub>2</sub>O<sub>3</sub> sensors for different gases. Concentration: 100 ppm; temperature: 500 °C.

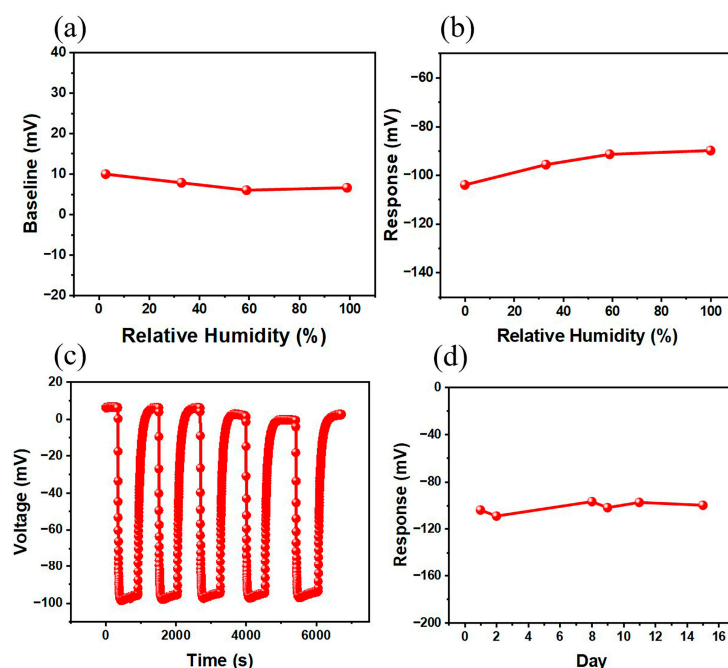


**Figure 8.** (a,b) Effect of humidity on (a) baseline and (b) response; (c) continuous dynamic response curves; and (d) stability test for PCO-Fe<sub>2</sub>O<sub>3</sub> sensor to 300 ppm H<sub>2</sub> at 500 °C.

#### 4. Discussion

For the widely adopted electrochemical (mixed-potential) mechanism, sensors usually exhibit a negative response to reducing gases such as H<sub>2</sub> [16]. When the chamber in which the SE is located contains only air, just one oxygen exchange reaction (OER) will occur on the TPB:



Upon the introduction of the analyte (H<sub>2</sub> in this case), a second electrochemical reaction takes place concurrently along with the OER, which is the hydrogen oxidation reaction (HOR):



The HOR reaction results in a change in electric charges in the double layer, which behaves similarly to a capacitor [27], thereby altering the electrode potential. As electrons are generated in the forward HOR, a negative contribution from the electrochemical mechanism to  $\Delta E$  (response) is yielded. Furthermore, the linear relationship between the response value and H<sub>2</sub> concentration or its logarithm and the power-law concentration dependence of response time for PCO-Fe<sub>2</sub>O<sub>3</sub> have also been observed for other electrode materials [14,28], in line with theoretical analyses based on mixed-potential theory [27,29]. Therefore, the non-Nernstian gas-sensing behavior of PCO-Fe<sub>2</sub>O<sub>3</sub> most probably follows the electrochemical mixed-potential mechanism.

Based on the mixed-potential mechanism, response values of sensors (absolute values) under Tafel kinetics can be expressed as [16,29]

$$S = \frac{b_{c,1}}{b_{c,1} + b_{a,2}} \Delta E^e + \frac{b_{c,1} b_{a,2}}{b_{c,1} + b_{a,2}} \lg \frac{i_2^0}{i_1^0} \quad (2)$$

where  $\Delta E^e = E_1^e - E_2^e$  is the thermodynamic equilibrium voltage (the difference in the equilibrium potentials between the OER and HOR),  $i_1^0$  and  $i_2^0$  are the exchange current for the OER and HOR, respectively, and  $b_{c,1}$  and  $b_{a,2}$  are the logarithmic cathodic tafel slope of the OER and the logarithmic anodic tafel slope of the HOR, respectively.

Taking into account the inverse relationship between exchange current density and polarization impedance ( $R_{c,1}$ ,  $R_{a,2}$ ), Equation (1) can be deformed as [30]

$$S = \frac{b_{c,1}}{b_{c,1} + b_{a,2}} \Delta E^e + \frac{b_{c,1} b_{a,2}}{b_{c,1} + b_{a,2}} \lg \frac{2R_{c,1}}{R_{a,2}} \quad (3)$$

where  $R_{c,1}$  and  $R_{a,2}$  represent the indicator of electroactivity for the OER and HOR of the sensing electrode material. Equations (2) and (3) indicate that materials of large  $i_2^0/i_1^0$  (or  $R_{c,1}/R_{a,2}$ ) are desirable for achieving a high response performance.

To measure the polarization resistances, symmetrical electrodes of PCO-Fe<sub>2</sub>O<sub>3</sub> were studied with impedance spectroscopy. The impedance spectra obtained typically consisted of two semicircles. The semicircle at high frequency corresponds to ohmic resistance, while the width of the semicircle at low frequency gives the polarization resistance. A large polarization impedance represents slow electrochemical kinetics.  $R_{c,1}$  and  $R_{a,2}$  were obtained from the low-frequency semicircle width of the impedance spectra tested in base air and oxygen-free H<sub>2</sub>/N<sub>2</sub>, respectively [16]. As shown in Figure 9,  $R_{c,1}$  is obviously much larger than  $R_{a,2}$ , indicating that the HOR is much more active than the OER. The H<sub>2</sub> response increased almost linearly with the increasing logarithmic  $R_{c,1}/R_{a,2}$ , in line with Equation (2). The variation of response with the activity ratio has been interpreted in terms of an electrochemical mixed-potential mechanism. For PCO-Fe<sub>2</sub>O<sub>3</sub>, the HOR activity is much larger than the OER one. Hence, the HOR competed strongly with the OER while the SE was exposed to an atmosphere containing H<sub>2</sub>, resulting in the significant cathodic polarization of the OER and thus a large response [29]. Furthermore,  $R_{a,2}$  decreased with the increase in H<sub>2</sub> concentration, suggesting the higher the H<sub>2</sub> concentration, the greater the HOR reaction rate will be. Thus, the response increased with increasing H<sub>2</sub> concentration.

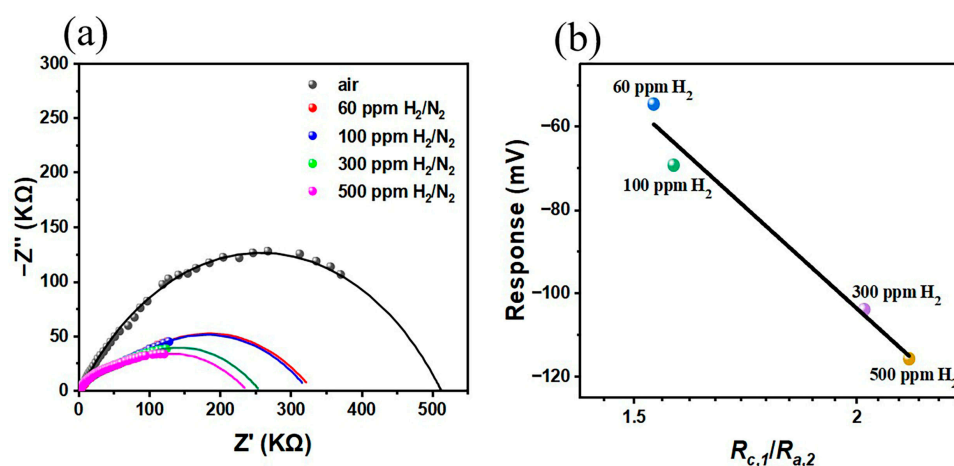


**Figure 9.** (a) Impedance spectra tested in different atmospheres for symmetrical PCO-Fe<sub>2</sub>O<sub>3</sub> at 500 °C. (b) Relationship between electrochemical activity ratio ( $R_{c,1}/R_{a,2}$ ) and response value.

The distribution of relaxation time (DRT) was applied to analyze, in detail, the impedance spectra of PCO-Fe<sub>2</sub>O<sub>3</sub> tested in air and H<sub>2</sub>/air to gain insight into changes in the electrochemical processes occurring at the electrode [31]. As shown in Figure 10a, the DRT plots obtained from the tests in each atmosphere can be divided into low-frequency (LF) peaks, intermediate-frequency (IF) peaks and high-frequency (HF) peaks, according to the frequency magnitude, which is consistent with the impedance fitting equivalent circuit plots. The literature suggests that these peaks correspond to different sub-processes or steps of OER for an MIEC electrode, i.e., the HF peak is associated with ionic transmission through the electrode/electrolyte intersection; the IF peak is related to charge transport on the electrode surface; and the LF peak is related to oxygen adsorption and diffusion on the electrode surface [32]. The magnitude of the peak area represents the resistance for the corresponding process, and a large peak corresponds to slow kinetics. As shown

in Figure 10a, the LF peak is obviously larger than IF and HF ones, which indicates that the oxygen adsorption and diffusion on the electrode surface associated with the LF peak play a determining role in the overall electrochemical reaction rate. In addition to this, we also observed that the intensity of the LF peak decreases when the SE is exposed to an atmosphere containing  $H_2$ . The LF peak significantly decreased in 60 ppm  $H_2$ , which became more pronounced as the  $H_2$  concentration increased. The IF peak also decreased in 60 ppm  $H_2$ /air, but the peak area remained almost constant afterwards, at higher  $H_2$  concentrations. Concerning the HF peak, no significant effect of  $H_2$  presence was observed. These results reveal that the enhanced electrochemical kinetics caused by  $H_2$ 's presence in air is mainly related to acceleration of the electrode surface processes.

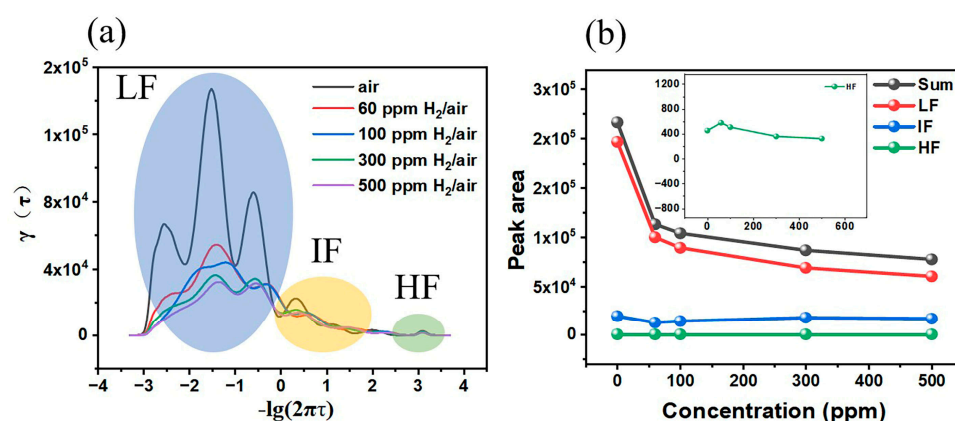


**Figure 10.** DRT analysis of PCO- $Fe_2O_3$  at 500 °C. (a) DRT plots; (b) variation of DRT peak area with  $H_2$  concentration, where the inset shows zoom-in of the HF curve.

When compared with reported non-Nernstian hydrogen sensors [14–17,28,33–38], PCO- $Fe_2O_3$  exhibited comparable  $H_2$  response characteristics (Table S1). In addition, for practical applications, hydrogen sensors need to meet a number of technical requirements. According to the US DOE (Department of Energy), stationary hydrogen sensors should be capable of detecting down to 1000 ppm of hydrogen with a response/recovery time of 30 s [39]. Although PCO- $Fe_2O_3$  meets the requirement for the detection limit and response time (at 500 °C), its recovery speed is insufficient. It is also noteworthy that hydrogen sensors operable at lower temperatures are most desirable, which can increase safety and reduce the power consumption of sensors. Further enhancement of the sensor performance is needed to meet these practical requirements, which may be achieved by optimizing the materials, including the electrode materials and morphology, oxide modifiers and solid electrolyte.

## 5. Conclusions

In this paper, a composite sensitive PCO- $Fe_2O_3$  electrode was fabricated using surface modification of a mixed-conducting PCO electrode with strongly acidic  $Fe_2O_3$ , and the potential response performance and electrochemical activity of PCO- $Fe_2O_3$  were investigated. Results showed that modification with strongly acidic  $Fe_2O_3$  led to a remarkable improvement in the  $H_2$ -sensing characteristics, including the response, sensitivity, LOD and response speed. The sensing behavior is in good agreement with the electrochemical mixed-potential mechanism. This enhanced  $H_2$  sensing by  $Fe_2O_3$  was primarily due to an increase in the ratio of electrochemical activity of hydrogen oxidation over oxygen reduction. In addition, the enhanced electrochemical kinetics caused by  $H_2$  presence in air is mainly related to acceleration of electrode surface processes. These findings show that acidic oxide surface modification may be an effective way to develop high-performance sensitive electrode materials.

**Supplementary Materials:** The following supporting information can be downloaded at: <https://www.mdpi.com/article/10.3390/chemosensors11040250/s1>. Figure S1: (a–d) Cross-section EDS mapping for PCO-Fe<sub>2</sub>O<sub>3</sub>; (e) Surface EDS quantification results of PCO-Fe<sub>2</sub>O<sub>3</sub>. Table S1: Comparison of H<sub>2</sub> sensing characteristics of PCO-Fe<sub>2</sub>O<sub>3</sub> with literature data.

**Author Contributions:** Conceptualization, J.Y.; investigation, L.W.; validation, L.W.; writing—original draft, L.W.; writing—review & editing, J.Y. and L.W.; funding acquisition, J.Y.; project administration, J.Y.; supervision, J.Y. All authors have read and agreed to the published version of the manuscript.

**Funding:** This work was supported by the National Key Research and Development Program of China (Grant 2021YFC3000300), the National Natural Science Foundation of China (Grant 62271462, 61871359), and Fundamental Research Funds for the Central Universities (Grant WK232000053).

**Institutional Review Board Statement:** Not applicable.

**Informed Consent Statement:** Not applicable.

**Data Availability Statement:** Data are available from authors upon request.

**Conflicts of Interest:** The authors declare no conflict of interest.

## References

1. Hassan, K.; Tung, T.T.; Yap, P.L.; Nine, M.J.; Kim, H.C.; Losic, D. Fast response hydrogen gas sensor based on Pd/Cr nanogaps fabricated by a single-step bending deformation. *Anal. Chim. Acta* **2020**, *1138*, 49–58. [[CrossRef](#)] [[PubMed](#)]
2. Buttner, W.J.; Post, M.B.; Burgess, R.; Rivkin, C. An overview of hydrogen safety sensors and requirements. *Int. J. Hydrog. Energy* **2011**, *36*, 2462–2470. [[CrossRef](#)]
3. Pak, Y.; Lim, N.; Kumaresan, Y.; Lee, R.; Kim, K.; Kim, T.H.; Kim, S.-M.; Kim, J.T.; Lee, H.; Ham, M.-H.; et al. Palladium Nanoribbon Array for Fast Hydrogen Gas Sensing with Ultrahigh Sensitivity. *Adv. Mater.* **2015**, *27*, 6945–6952. [[CrossRef](#)] [[PubMed](#)]
4. Gutmacher, D.; Hoefler, U.; Wöllenstein, J. Gas sensor technologies for fire detection. *Sens. Actuators B Chem.* **2012**, *175*, 40–45. [[CrossRef](#)]
5. Hübert, T.; Boon-Brett, L.; Black, G.; Banach, U. Hydrogen sensors—A review. *Sens. Actuators B Chem.* **2011**, *157*, 329–352. [[CrossRef](#)]
6. Toribio, J.; Lorenzo, M.; Aguado, L. Innovative Design of Residual Stress and Strain Distributions for Analyzing the Hydrogen Embrittlement Phenomenon in Metallic Materials. *Materials* **2022**, *15*, 9063. [[CrossRef](#)]
7. Chauhan, P.S.; Bhattacharya, S. Hydrogen gas sensing methods, materials, and approach to achieve parts per billion level detection: A review. *Int. J. Hydrogen Energy* **2019**, *44*, 26076–26099. [[CrossRef](#)]
8. Shen, B.; Luo, J.; Xie, Y.; Zhang, D.; Fan, P.; Zhong, A. Hydrogen gas ppb-level detection based on AlGa<sub>N</sub>/Ga<sub>N</sub> high electron mobility transistor with 2.0 nm thick Pt gate layer. *Appl. Phys. Lett.* **2019**, *115*, 254104. [[CrossRef](#)]
9. Podlepetsky, B.; Samotaev, N.; Kovalenko, A. Responses' parameters of hydrogen sensors based on MISFET with Pd(Ag)-Ta<sub>2</sub>O<sub>5</sub>-SiO<sub>2</sub>-Si structure. *Sens. Actuators B Chem.* **2019**, *290*, 698–705. [[CrossRef](#)]
10. Ivanov, I.I.; Baranov, A.M.; Talipov, V.A.; Mironov, S.M.; Akbari, S.; Kolesnik, I.V.; Orlova, E.D.; Napolskii, K.S. Investigation of catalytic hydrogen sensors with platinum group catalysts. *Sens. Actuators B Chem.* **2021**, *346*, 130515. [[CrossRef](#)]
11. Wu, R.-J.; Tian, X.-M.; Hua, Z.-Q.; Lu, N.; Wang, P. A low temperature catalytic combustible gas sensor based on Ru supported zeolite catalyst films. *Chin. J. Anal. Chem.* **2021**, *49*, 63–68. [[CrossRef](#)]
12. Bhardwaj, A.; Kumar, A.; Bae, H.; Park, C.J.; Song, S.J. Surface decorated spinel-oxide electrodes for mixed-potential ammonia sensor: Performance and DRT analysis. *J. Hazard Mater.* **2020**, *396*, 122601. [[CrossRef](#)] [[PubMed](#)]
13. Wang, B.; Liu, F.; Yang, X.; Guan, Y.; Ma, C.; Hao, X.; Liang, X.; Liu, F.; Sun, P.; Zhang, T.; et al. Fabrication of Well-Ordered Three-Phase Boundary with Nanostructure Pore Array for Mixed Potential-Type Zirconia-Based NO<sub>2</sub> Sensor. *ACS Appl. Mater. Interfaces* **2016**, *8*, 16752–16760. [[CrossRef](#)] [[PubMed](#)]
14. Zhang, H.; Yi, J.; Jiang, X. Fast Response, Highly Sensitive and Selective Mixed-Potential H<sub>2</sub> Sensor Based on (La, Sr)(Cr, Fe)O<sub>3-δ</sub> Perovskite Sensing Electrode. *ACS Appl. Mater. Interfaces* **2017**, *9*, 17218–17225. [[CrossRef](#)] [[PubMed](#)]
15. Anggraini, S.A.; Ikeda, H.; Miura, N. Tuning H<sub>2</sub> Sensing Performance of Zirconia-based Sensor using ZrSiO<sub>4</sub>(+Au) Sensing-electrode. *Electrochim. Acta* **2015**, *171*, 7–12. [[CrossRef](#)]
16. Zhang, H.; Yi, J.; Zhang, Z.; Zhang, H. The relation between mixed-potential hydrogen response and electrochemical activities for perovskite oxides. *Sens. Actuators B Chem.* **2022**, *352*, 130988. [[CrossRef](#)]
17. Miura, N.; Sato, T.; Anggraini, S.A.; Ikeda, H.; Zhuiykov, S. A review of mixed-potential type zirconia-based gas sensors. *Ionics* **2014**, *20*, 901–925. [[CrossRef](#)]
18. Zhang, Z.; Yi, J.; Han, H.; Meng, Y.; Zhang, H.; Jiang, Y. Electrochemical Response of Mixed Conducting Perovskite Enables Low-Cost High-Efficiency Hydrogen Sensing. *ACS Appl. Mater. Interfaces* **2022**, *14*, 33580–33588. [[CrossRef](#)]

19. Lu, Q.; Huang, L.; Hao, X.; Li, W.; Wang, B.; Wang, T.; Liang, X.; Liu, F.; Wang, C.; Lu, G. Mixed potential type NH<sub>3</sub> sensor based on YSZ solid electrolyte and metal oxides (NiO, SnO<sub>2</sub>, WO<sub>3</sub>) modified FeVO<sub>4</sub> sensing electrodes. *Sens. Actuators B Chem.* **2021**, *343*, 130043. [[CrossRef](#)]
20. Lu, G.; Miura, N.; Yamazoe, N. High-temperature hydrogen sensor based on stabilized zirconia and a metal oxide electrode. *Sens. Actuators B Chem.* **1996**, *35*, 130–135. [[CrossRef](#)]
21. Liu, T.; Zhang, X.; Yuan, L.; Yu, J. A review of high-temperature electrochemical sensors based on stabilized zirconia. *Solid State Ion.* **2015**, *283*, 91–102. [[CrossRef](#)]
22. Nicollet, C.; Toparli, C.; Harrington, G.F.; Defferriere, T.; Yildiz, B.; Tuller, H.L. Acidity of surface-infiltrated binary oxides as a sensitive descriptor of oxygen exchange kinetics in mixed conducting oxides. *Nat. Catal.* **2020**, *3*, 913–920. [[CrossRef](#)]
23. Li, J.; Lu, Y.; Ye, Q.; Cinke, M.; Han, J.; Meyyappan, M. Carbon Nanotube Sensors for Gas and Organic Vapor Detection. *Nano Lett.* **2003**, *3*, 929–933. [[CrossRef](#)]
24. Balamurugan, S.; Naresh, N.; Prakash, I.; Satyanarayana, N. Capacity fading mechanism of Li<sub>2</sub>O loaded NiFe<sub>2</sub>O<sub>4</sub>/SiO<sub>2</sub> aerogel anode for lithium-ion battery: Ex-situ XPS analysis. *Appl. Surf. Sci.* **2021**, *535*, 147677. [[CrossRef](#)]
25. Fan, Y.; Wang, W.; Zhang, J.; Lu, Y.; Liu, C.; Adimi, S.; Zhou, J.; Ruan, S.; Chen, Y. Construction of p-n heterojunctions by modifying MOF-derived  $\alpha$ -Fe<sub>2</sub>O<sub>3</sub> with partially covered cobalt tungstate for high-performance ethyl acetate detection. *Sens. Actuators B Chem.* **2021**, *344*, 130129. [[CrossRef](#)]
26. Yan, W.; Fan, H.; Zhai, Y.; Yang, C.; Ren, P.; Huang, L. Low temperature solution-based synthesis of porous flower-like  $\alpha$ -Fe<sub>2</sub>O<sub>3</sub> superstructures and their excellent gas-sensing properties. *Sens. Actuators B Chem.* **2011**, *160*, 1372–1379. [[CrossRef](#)]
27. Zhang, J.; Zhang, H.; Teng, Y.; Yi, J. Simulation of dynamic response of mixed-potential hydrogen sensors. *Int. J. Hydrog. Energy* **2022**, *47*, 33891–33902. [[CrossRef](#)]
28. Yi, J.; Zhang, H.; Zhang, Z.; Chen, D. Hierarchical porous hollow SnO<sub>2</sub> nanofiber sensing electrode for high performance potentiometric H<sub>2</sub> sensor. *Sens. Actuators B Chem.* **2018**, *268*, 456–464. [[CrossRef](#)]
29. Yi, J.; Han, H. Analysis of factors affecting response for mixed potential gas sensors. *Electrochim. Acta* **2021**, *379*, 138129. [[CrossRef](#)]
30. Liu, Q.; Dong, X.; Xiao, G.; Zhao, F.; Chen, F. A Novel Electrode Material for Symmetrical SOFCs. *Adv. Mater.* **2010**, *22*, 5478–5482. [[CrossRef](#)]
31. Lu, M.Y.; Scipioni, R.; Park, B.-K.; Yang, T.; Chart, Y.A.; Barnett, S.A. Mechanisms of PrOx performance enhancement of oxygen electrodes for low and intermediate temperature solid oxide fuel cells. *Mater. Today Energy* **2019**, *14*, 100362. [[CrossRef](#)]
32. Adler, S.B. Factors Governing Oxygen Reduction in Solid Oxide Fuel Cell Cathodes. *Chem. Rev.* **2004**, *104*, 4791–4844. [[CrossRef](#)] [[PubMed](#)]
33. Sekhar, P.K.; Brosha, E.L.; Mukundan, R.; Nelson, M.A.; Williamson, T.L.; Garzon, F.H. Development and testing of a miniaturized hydrogen safety sensor prototype. *Sens. Actuators B Chem.* **2010**, *148*, 469–477. [[CrossRef](#)]
34. Anggraini, S.A.; Breedon, M.; Miura, N. Sensing characteristics of aged zirconia-based hydrogen sensor utilizing Zn-Ta-based oxide sensing-electrode. *Electrochem. Commun.* **2013**, *31*, 133–136. [[CrossRef](#)]
35. Tang, Z.; Li, X.; Yang, J.; Yu, J.; Wang, J.; Tang, Z. Mixed potential hydrogen sensor using ZnWO<sub>4</sub> sensing electrode. *Sens. Actuators B Chem.* **2014**, *195*, 520–525. [[CrossRef](#)]
36. Li, Y.; Li, X.; Tang, Z.; Tang, Z.; Yu, J.; Wang, J. Hydrogen sensing of the mixed-potential-type MnWO<sub>4</sub>/YSZ/Pt sensor. *Sens. Actuators B Chem.* **2015**, *206*, 176–180. [[CrossRef](#)]
37. Li, Y.; Li, X.; Tang, Z.; Wang, J.; Yu, J.; Tang, Z. Potentiometric hydrogen sensors based on yttria-stabilized zirconia electrolyte (YSZ) and CdWO<sub>4</sub> interface. *Sens. Actuators B Chem.* **2016**, *223*, 365–371. [[CrossRef](#)]
38. Li, Y.; Li, X.; Wang, J.; Jun, Y.; Tang, Z. A cobalt tungstate compound sensing electrode for hydrogen detection based upon mixed-potential type sensors. *RSC Adv.* **2017**, *7*, 2919–2925. [[CrossRef](#)]
39. Darmadi, I.; Nugroho, F.A.A.; Langhammer, C. High-Performance Nanostructured Palladium-Based Hydrogen Sensors—Current Limitations and Strategies for Their Mitigation. *ACS Sens.* **2020**, *5*, 3306–3327. [[CrossRef](#)]

**Disclaimer/Publisher’s Note:** The statements, opinions and data contained in all publications are solely those of the individual author(s) and contributor(s) and not of MDPI and/or the editor(s). MDPI and/or the editor(s) disclaim responsibility for any injury to people or property resulting from any ideas, methods, instructions or products referred to in the content.